Performance of Under–resolved Two–Dimensional Incompressible Flow Simulations [1] [2]

David L. Brown
Computing, Information and Communications Division
Los Alamos National Laboratory
Los Alamos, New Mexico, USA

Michael L. Minion
Courant Institute of Mathematical Sciences
New York University
251 Mercer Street
New York, NY 10012

Revised: February 10, 1995

[1]This work performed under the auspices of the U.S. Department of Energy by Los Alamos National Laboratory under Contract W-7405-ENG-36.

Pages: 40
Figures: 13
Tables: 6
Subject Classification Index Numbers: 65M10, 76–08, 76D05
Keywords: Incompressible Flow, Difference Approximations, Projection Methods, Pressure Poisson, Numerical Accuracy

Suggested Running Head: Under–resolved Incompressible Flow Simulations

All corresponcence to:
David L. Brown
Mail Stop B265
Los Alamos National Laboratory
Los Alamos, NM 87545
Phone: (505) 667–0120
Fax: (505) 665–5220
Email: dlb@lanl.gov

Abstract

A careful study of the behavior of a Godunov-projection method for the incompressible Navier-Stokes equations as a function of the resolution of the computational mesh is presented. By considering a representative example problem, it is demonstrated that a Godunov-projection method performs as well as an accurate centered finite difference method in cases where the smallest flow scales are well-resolved. In under-resolved cases, however, where centered methods compute solutions badly polluted with mesh-scale oscillations, the Godunov-projection method sometimes computes smooth, apparently physical solutions. Closer examination indicates that these under-resolved Godunov solutions, although convergent when the grid is refined, contain spurious non-physical vortices that are artifacts of the under-resolution. These artifacts are not unique to Godunov methods, however, and are observed with other difference approximations as well. The implication of these results on the applicability of difference approximations to engineering flow problems in the under-resolved case is discussed.

Contents

List of Figures

List of Tables

1 Introduction.

In 1989, Bell, Colella and Glaz [1] introduced a projection method for the incompressible Navier-Stokes equations that combines the projection technique introduced by Chorin [2] and Colella's higher-order Godunov advection schemes [3] to give an overall second-order finite difference method. This method has been demonstrated to have very attractive properties for large scale modeling of incompressible or nearly incompressible engineering flows. In the succeeding years, Bell, Colella and their coworkers have introduced several variants of the original Bell-Colella-Glaz formulation, including methods that use an "approximate" projection operator [4] , extensions to chemically reacting flows [5] [6], and modifications for adaptive mesh refinement [7]. Because the Godunov upwinding approach stabilizes the computed flows for cell Reynolds numbers where a strictly centered finite difference scheme would produce spurious mesh-size oscillations and often instability, these Godunov-projection methods would appear to offer the hope to the design engineer of being able to make routine simulations in situations where it is not possible to carefully resolve the smallest scales everywhere in the computed flows. With currently available computing machines, such under-resolution is often unavoidable. An example is the solution of problems of any realistic complexity in three space dimensions. In regions of the flow where the physical viscosity is too small to be captured properly by the finite difference method, the Godunov upwinding is expected to "do the right thing" by representing near-discontinuities with appropriately smoothed but sufficiently sharp features that maintain the basic appearance, and hopefully the physical properties of the actual physical flow. It is the aim of the present paper to address the issue of whether such under-resolved computations using Godunov-based methods can be expected to faithfully represent the correct physical behavior of the fluid flow. Although resolved computations using a higher-order accurate central difference approximation to the incompressible Navier-Stokes equations are used in this paper to provide reference solutions, this paper is not intended to provide a comparison between Godunov methods and other methods, but mainly addresses the issue of the reliability of Godunov methods. We note that a study with somewhat

similar objectives was done by E and Shu for some ENO-type schemes [8].

Although not the main focus of that paper, the authors of [1] briefly discuss the issue of whether under-resolved problems can be computed in some reasonable way using Godunov-projection methods. As they also state, the justification typically given for the physical correctness of such calculations is that if the structure of the computed solutions is essentially correct (shear layer placement, etc.), then the numerical dissipation mechanisms in the finite difference scheme will mimic the physical dissipation mechanisms, leading to results with the correct large-scale dynamics. The computational examples presented in [1] for the evolution of an infinitely thin shear layer offer "food for thought", but no conclusive evidence for this proposition. In [9], Bell and Marcus present a computational study of three–dimensional vortex evolution, in which they are somewhat more cautious in the interpretation of their results at later times as the dynamics of the solution become more complicated. Since the infinitely thin shear layer problem is an extremely difficult one to attack both numerically and theoretically, we instead consider a related "thin" shear layer problem. As will become apparent below, our computations cast doubt on the validity of the proposition that the numerical dissipation mechanisms in Godunov-projection methods mimic the physical dissipation.

With the idea in mind of improving the understanding of the numerical dissipation mechanisms in Godunov-projection methods, we present a set of carefully controlled numerical experiments designed to investigate situations where the smallest scales of the flow are well-resolved, and situations where they are not. The test cases studied are variations on the finitely-thick double shear layer problem in a doubly periodic domain presented by Bell, Colella and Glaz in their introductory paper [1]. The version of the projection method used in this paper is the one introduced by Bell, Colella and Howell [10]. While the results presented in this study by no means represent an exhaustive study, the thin shear layer is an important feature in practical engineering situations, since as a basically unstable structure, it represents one of the important mechanisms for fluid mixing. The reference solutions used for comparisons are computed with a cen-

tered, finite-difference, vorticity stream-function method that is fourth-order accurate in both space and time. The fourth-order Runge-Kutta time integrator adds a negligible amount of dissipation to the method, and no artificial spatial viscosity is used, so the dominant dissipation mechanism in the method comes from the physical viscosity terms. Carefully controlled convergence studies of the centered method demonstrate that these are valid reference solutions.

The basic conclusions that can be drawn from the present study are the following:

- For problems in which the smallest physical scales are well-resolved, the solutions produced by the Godunov-projection and fourth-order centered difference methods are virtually indistinguishable. The effective artificial viscosity introduced by the Godunov upwinding appears to be negligible compared with the physical viscosity terms, as evidenced by the plots of energy and enstrophy dissipation for the methods. Visual inspection, convergence studies, and direct numerical comparison with the reference solutions indicate that the Godunov solutions faithfully represent the true Navier-Stokes solutions.

- For problems in which the smallest physical scales are not well-resolved, the appearance of the Godunov solutions is often qualitatively different than that of the reference solutions. While in the correct solution, each shear layer rolls up into a single periodically-repeated vortex, the under-resolved solutions can also exhibit additional vortex roll-ups between the main vortices. At first glance, these additional vortices might appear to be well–resolved features of the flow. However, there are several important observations that demonstrate that these are actually numerical artifacts. The additional vortices represent only small perturbations of energy and enstrophy in the flow. Also, as the mesh size is refined, the amplitude of the additional vortices decreases, although not at the second order rate that might be expected of the method. Once the layers are sufficiently resolved by the mesh, these artifacts disappear. We also present evidence to suggest that these artifacts are not solely a property of Godunov type methods. Indeed, it is possible to produce artifacts of similar appearance even with a centered dif-

ference approximation. Thus we conclude that the artifacts are a function of under-resolution rather than a defect in the fundamental design of the Godunov difference approximation.

In section 2, the Godunov-projection method is introduced, as well as the the fourth-order centered-difference method used to compute the reference solutions. Section 3 describes the computations and convergence studies. Speculations on the implications of these artifacts to engineering simulations are presented in section 4.

2 The numerical methods.

In two space dimensions the incompressible Navier-Stokes equations can be written as

$$U_t + (U \cdot \nabla)U + \nabla p = \nu \Delta U \tag{1}$$

$$\nabla \cdot U = 0, \tag{2}$$

where $U = (u, v)^T = U(x, y, t)$ is the fluid velocity vector with components u and v, the horizontal and vertical velocity, respectively, $p = p(x, y, t)$ is the fluid pressure, ν is the (assumed constant) fluid viscosity, and subscripts denote partial differentiation. An equivalent formulation can be written using the Hodge decomposition theorem, which states that any vector field W can be decomposed into two parts, one of which is divergence-free and the other solenoidal. Moreover, these components are orthogonal (see *e.g.* Chorin [2]).

$$W = U + \nabla\phi, \qquad U = \mathbf{P}W, \qquad \nabla\phi = (\mathbf{I} - \mathbf{P})W, \tag{3}$$

where $\mathbf{P}$ is the implied projection operator that decomposes the field. Using $\mathbf{P}$, the momentum equation can be written as

$$U_t = \mathbf{P}\left\{-(U \cdot \nabla)U + \nu \Delta U\right\} \tag{4}$$

$$\nabla p = (\mathbf{I} - \mathbf{P})\left\{-(U \cdot \nabla)U + \nu \Delta U\right\}. \tag{5}$$

Another formulation can be written by using the vorticity ω and stream function ψ as dependent variables. The vorticity is defined as the curl of the velocity field,

$$\omega = \nabla \times U \tag{6}$$

which is a scalar, for the two space-dimensional case, and the stream function satisfies the Cauchy-Riemann equations,

$$(u, v) =: (\psi_y, -\psi_x). \tag{7}$$

In these variables, the incompressible Navier-Stokes equations are given by

$$\omega_t = -(u\omega)_x - (v\omega)_y + \nu\Delta\omega \tag{8}$$

$$\Delta\psi = -\omega. \tag{9}$$

The Navier-Stokes equations require that boundary conditions be specified. The examples presented in this paper are for a doubly periodic domain and hence the only boundary condition required is that the solutions be doubly periodic.

2.1 Computational Domain

Both of the numerical methods in this paper are implemented on the same computational grid. The physical domain in all problems is the periodic unit square. We use a 2^N by 2^N square grid, with uniform cell size $h = 1/2^N$ for our spatial discretization. Unless otherwise noted, all variables are cell centered, i.e. the grid location (i, j) corresponds to the physical location $((i - \frac{1}{2})h, (j - \frac{1}{2})h)$.

2.2 The Godunov-projection method of Bell, Colella and Howell.

The projection method employed in the numerical studies in this paper is essentially the same as the one introduced in [10]. For completeness, and also to correct some typographical errors in the original publication, the details of the method are presented here. In this projection method, the velocities and pressure are computed in several steps. In the first step, a non-divergence free prediction of the velocity U^* is computed:

$$\frac{U^* - U^n}{\Delta t} = \frac{\nu}{2}\Delta_h(U^n + U^*) - [(U \cdot \nabla)U]^{n+1/2} - \nabla p^{n-1/2}, \tag{10}$$

where Δ_h is the standard five-point central difference approximation to the Laplacian operator, and $\nabla p^{n-1/2}$ is the time-centered pressure gradient which we assume is available from the previous time step. The advection term $[(U \cdot \nabla)U]^{n+1/2}$ is approximated

by a Godunov procedure, also described in detail below. For $\nu \neq 0$, the numerical solution of (10) involves the solution of a heat-like equation; this is done using a multigrid iteration.

Next, in the "projection" step of the method, the value of U^* is decomposed into the sum of a divergence free part U^{n+1} and the gradient of a scalar field ϕ, that are then used to update the velocity and the pressure gradient.

$$U^* = U^{n+1} + \nabla\phi \tag{11}$$

$$\nabla p^{n+\frac{1}{2}} = \nabla p^{n-\frac{1}{2}} + \frac{\nabla\phi}{\Delta t} \tag{12}$$

where ϕ is determined by solving the Poisson equation

$$\Delta\phi = \nabla \cdot U^*. \tag{13}$$

The form of the projection operator $\mathbf{P}$ can be completely specified by the choice of the discrete divergence operator D. Given a choice for D, the discrete gradient operator can be defined as the adjoint of D which insures that $\mathbf{P}$ is well-posed and norm reducing. (see e.g. Chorin [11]). The centered-difference approximation to the divergence

$$D(U)_{i,j} = \frac{(u_{i+1,j} - u_{i-1,j}) + (v_{i,j+1} - v_{i,j-1})}{2h} \tag{14}$$

is used, which has as its adjoint the centered-difference gradient

$$G(\phi)_{i,j} = (\frac{\phi_{i+1,j} - \phi_{i-1,j}}{2h}, \frac{\phi_{i,j+1} - \phi_{i,j-1}}{2h}). \tag{15}$$

This gives for the discrete form of equation (13),

$$L(\phi) = D(U), \tag{16}$$

where

$$L(\phi)_{i,j} = DG(\phi)_{i,j} = \frac{-4\phi_{i,j} + \phi_{i+2,j} + \phi_{i-2,j} + \phi_{i,j+2} + \phi_{i,j-2}}{4h^2} \tag{17}$$

Because the stencil of the operator L decouples into four distinct substencils, the null-space of L contains any vector that is constant on each of the stencils. An adaptation of the standard multigrid method that respects the decoupling in the interpolation,

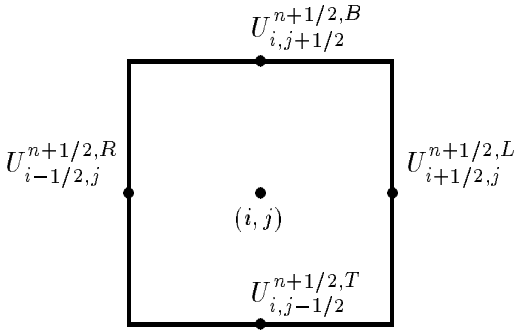

Figure 1: Location of Cell variables. The cell center is located at (i, j). Cell edge values are denoted using half-integer indices. For example, a cell edge value extrapolated from the left to the right cell face at time level $n + \frac{1}{2}$ is denoted by $U^{n+1/2,L}_{i+1/2,j}$

averaging, and relaxation operators is used to solve equation (16). This insures that high frequency errors on each decoupled stencil are adequately reduced during each multigrid sweep. Details of this technique are found in [10].

The approximation of the time centered advective term $[(U \cdot \nabla)U]^{n+1/2}$ uses a second-order Godunov procedure. The basic idea of the procedure is to use a Taylor series expansion to calculate time-centered cell edge values of the velocities that can then be differenced to yield the advective term. As an example, we consider how the value on the left side of the cell face centered at $(i + \frac{1}{2}, j, n + \frac{1}{2})$, $U^{n+\frac{1}{2},L}_{i+\frac{1}{2},j}$, is computed; the values on each side of the other faces are computed analogously.

The leading terms of the Taylor series are used to extrapolate the velocities to cell edges (see figure 1 for location of cell edge variables).

$$U^{n+1/2,L}_{i+1/2,j} = U^n_{i,j} + \tfrac{h}{2}(U^n_x)_{i,j} + \tfrac{\Delta t}{2}(U^n_t)_{i,j}. \tag{18}$$

By using the Navier-Stokes equations, the temporal derivatives are replaced with spatial derivatives yielding

$$\begin{aligned} U^{n+1/2,L}_{i+1/2,j} \quad = U^n_{i,j} \quad & +[\tfrac{h}{2} - \tfrac{\Delta t}{2}u^n_{i,j}](U^n_x)_{i,j} - \tfrac{\Delta t}{2}v^n_{i,j}(U^n_y)_{i,j} \\ & +\tfrac{\Delta t}{2}\nu(\Delta U^n)_{i,j} - \tfrac{\Delta t}{2}\nabla p^n_{i,j} \end{aligned} \tag{19}$$

This is approximated in three steps. First predicted edge values $\hat{U}^L$ of the velocity are computed which contain only the derivative terms from (19) normal to the cell

edge.

$$\begin{aligned} \hat{U}^L_{i+1/2,j} &= U^n_{i,j} + [\tfrac{h}{2} - s_L \tfrac{\Delta t}{2} u^n_{i,j}](U^n_x)_{i,j} \\ s_L &= \begin{cases} 1 & \text{if } u_{i,j} > 0 \\ 0 & \text{otherwise} \end{cases} \end{aligned} \tag{20}$$

The term $(U^n_x)_{i,j}$ is approximated using fourth order monotonicity preserving slopes (see below). A similar procedure extrapolates from the right in the cell centered at $i+1, j$ to obtain $\hat{U}^{n+\frac{1}{2},R}_{i+\frac{1}{2},j}$ A method based on the Riemann problem for Burgers' equation is used to resolve this ambiguity:

$$\hat{U}^{n+\frac{1}{2}}_{i-1/2,j} = \begin{cases} \hat{U}^{n+\frac{1}{2},L}_{i-1/2,j} & \text{if } u^n_{i,j} > 0, u^n_{i-1,j} > 0 \\ \hat{U}^{n+\frac{1}{2},R}_{i-1/2,j} & \text{if } u^n_{i,j} < 0, u^n_{i-1,j} < 0 \\ (\hat{U}^{n+\frac{1}{2},L}_{i-1/2,j} + \hat{U}^{n+\frac{1}{2},R}_{i-1/2,j})/2 & \text{otherwise} \end{cases} \tag{21}$$

is chosen.

The fourth-order limited difference for approximating the normal derivative term in equation (20) is given by the following. Define the difference operators

$$\begin{aligned} D^c(\phi)_{i,j} &= (\phi_{i+1,j} - \phi_{i-1,j})/2 \\ D^l(\phi)_{i,j} &= (\phi_{i,j} - \phi_{i-1,j}) \\ D^r(\phi)_{i,j} &= (\phi_{i+1,j} - \phi_{i,j}) \end{aligned}$$

Using these, define

$$\begin{aligned} \delta^{lim}(\phi)_{i,j} &= \begin{cases} min(2|D^l(\phi)_{i,j}|, 2|D^r(\phi)_{i,j}|) & \text{if } (D^l(\phi)_{i,j})(D^r(\phi)_{i,j}) > 0 \\ 0 & \text{otherwise} \end{cases} \\ \delta^f(\phi)_{i,j} &= min(|D^c(\phi)_{i,j}|, \delta^{lim}(\phi)_{i,j}) \times sign(D^c(\phi)_{i,j}) \end{aligned}$$

and

$$\delta(\phi)_{i,j} = min(|\frac{4(D^c(\phi)_{i,j})}{3} - \frac{(\delta^f(\phi)_{i+1,j} + \delta^f(\phi)_{i-1,j})}{6}|, \delta^{lim}(\phi)_{i,j}) \times sign(D^c(\phi)_{i,j})$$

Then, the derivative is approximated with

$$(\phi_x)_{i,j} \approx \delta(\phi)_{i,j}/\Delta x.$$

The second step is to add the viscous and the transverse derivative term in (20) to yield edge values $\tilde{U}$. A standard five-point approximation to the Laplacian for the viscous term is used and a difference of the computed value $\hat{U}$ is used to form the transverse derivative term. Thus

$$\begin{aligned} \tilde{U}^L_{i+\frac{1}{2},j} &= \hat{U}^L_{i+\frac{1}{2},j} - \tfrac{\Delta t}{2}(\widehat{(vU_y)}_{i,j}) + \tfrac{\Delta t}{2}\nu(\Delta^5(U^n)_{i,j} \\ \widehat{(vU_y)}_{i,j} &= \frac{(\hat{v}_{i,j+1/2} + \hat{v}_{i,j-1/2})}{2}\frac{(\hat{U}_{i,j+1/2} - \hat{U}_{i,j-1/2})}{\Delta y} \end{aligned} \tag{22}$$

Edge values $\tilde{U}^{n+\frac{1}{2}}_{i+\frac{1}{2},j}$ are then determined from the left and right states using the analogous formula to (21). To complete the approximation of time centered cell edge values, the pressure gradient term from equation (19) must be included. This is approximated by performing a MAC-projection on the computed values $\tilde{U}_{i,j}$ [10]. We solve

$$\Delta^5(\phi) = D^M(\tilde{U})_{i,j} = \frac{(\tilde{u}_{i+1/2,j} - \tilde{u}_{i-1/2,j})}{h} + \frac{(\tilde{v}_{i,j+1/2} - \tilde{v}_{i,j-1/2})}{h} \tag{23}$$

where Δ^5 is the standard five-point Laplacian approximation, and then subtract the gradient of ϕ from $\tilde{U}^{n+\frac{1}{2}}_{i,j}$ to form $U^{n+\frac{1}{2}}_{i+\frac{1}{2},j}$ and $U^{n+\frac{1}{2}}_{i,j+\frac{1}{2}}$:

$$\begin{aligned} u^{n+1/2}_{i+1/2,j} &= \tilde{u}^{n+1/2}_{i+1/2,j} - \frac{\phi_{i+1,j} - \phi_{i,j}}{h} \\ v^{n+1/2}_{i+1/2,j} &= \tilde{v}^{n+1/2}_{i+1/2,j} - \frac{(\phi_{i,j+1} + \phi_{i+1,j+1})/2 - (\phi_{i,j-1} + \phi_{i+1,j-1})/2}{2h}. \end{aligned}$$

Finally, the values $U^{n+1/2}$ are differenced to get the advection term:

$$\begin{aligned} (uU_x + vU_y)_{i,j} &= \frac{(u^{n+\frac{1}{2}}_{i+1/2,j} + u^{n+\frac{1}{2}}_{i-1/2,j})}{2}\frac{(U^{n+\frac{1}{2}}_{i+1/2,j} - U^{n+\frac{1}{2}}_{i-1/2,j})}{h} \\ &+ \frac{(v^{n+\frac{1}{2}}_{i,j+1/2} + v^{n+\frac{1}{2}}_{i,j-1/2})}{2}\frac{(U^{n+\frac{1}{2}}_{i,j+1/2} - U^{n+\frac{1}{2}}_{i,j-1/2})}{h} \end{aligned}$$

2.3 The fourth-order centered difference approximation.

The reference solutions used for this study were computed using a fourth-order accurate hybrid finite-difference/spectral approximation of the vorticity stream-function formulation of the Navier-Stokes equations (8,9). For the approximation of the hybrid method, the same computational grid is used as in the previous section. Values of the

vorticity, velocities, and stream function are given at each cell center. The right hand side of equation (8) is approximated with fourth order finite differences. Specifically,

$$(\omega_t)_{i,j} = -D_x^4(u\omega)_{i,j} - D_y^4(v\omega)_{i,j} + \nu\Delta^4(\omega)_{i,j} \tag{24}$$

where the difference operators $D_{x,y}^4$ are defined by

$$\begin{aligned} D_x^4(\phi)_{i,j} &= \frac{\phi_{i-2,j} - 8(\phi_{i-1,j} - \phi_{i+1,j}) - \phi_{i+2,j}}{12h} \\ D_y^4(\phi)_{i,j} &= \frac{\phi_{i,j-2} - 8(\phi_{i,j-1} - \phi_{i,j+1}) - \phi_{i,j+2}}{12h} \end{aligned}$$

and the approximation to the Laplacian is given by

$$\begin{aligned} \Delta^4(\phi)_{i,j} &= D_{xx}^4(\phi)i,j + D_{yy}^4(\phi)i,j \\ D_{xx}^4(\phi)i,j &= \frac{-30\phi_{i,j} + 16(\phi_{i-1,j} + \phi_{i+1,j}) - (\phi_{i-2,j} + \phi_{i+2,j})}{12h^2} \\ D_{yy}^4(\phi)i,j &= \frac{-30\phi_{i,j} + 16(\phi_{i,j-1} + \phi_{i,j+1}) - (\phi_{i,j-2} + \phi_{i,j+2})}{12h^2} \end{aligned}$$

A standard, fourth-order Runge-Kutta method is used to advance the solution in time. Specifically, let

$$F(\omega, u, v)_{i,j} = -D_x^4(u\omega)_{i,j} - D_y^4(v\omega)_{i,j} + \nu\Delta^4(\omega)_{i,j}, \tag{25}$$

then the time-stepping procedure can be written as

$$\begin{aligned} \omega^1 &= \omega^n + \tfrac{\Delta t}{2} F(\omega^n, u^n, v^n) \\ \omega^2 &= \omega^n + \tfrac{\Delta t}{2} F(\omega^1, u^1, v^1) \\ \omega^3 &= \omega^n + \Delta t F(\omega^2, u^2, v^2) \\ \omega^{n+1} &= \frac{-\omega^n + \omega^1 + 2\omega^2 + \omega^3}{3} + \frac{\Delta t}{6} F(\omega^3, u^3, v^3) \end{aligned}$$

At each of the four Runge-Kutta substeps, the velocities must be recomputed from the vorticity. The first step in doing so is to discretize the Poisson problem (9) and solve the resulting problem for the stream function ψ. Since the domain is doubly periodic, it is convenient to solve (9) in Fourier space. The true inverse Laplacian operator is used and no additional spectral filtering is employed. Hence

$$\psi(x, y) = \sum_{j,k=-\frac{N}{2}+1}^{\frac{N}{2}} \frac{\hat{\omega}_{j,k}}{j^2 + k^2} e^{2\pi i(jx+ky)} \tag{26}$$

where $\hat{\omega}_{j,k}$ are the discrete Fourier coefficients of the vorticity.

Since the spectral Laplacian involves only real numbers, a real to real FFT is used in lieu of a complex FFT which reduces the computational cost of the FFT by approximately one half. Even with this savings, approximately 70% of the total computational cost of the method involves solving equation (9) on a Cray YMP.

Once ψ has been computed, the difference operators from above are used to compute the velocities.

$$\begin{aligned} u_{i,j} &= D_y^4(\psi)_{i,j} \\ v_{i,j} &= -D_x^4(\psi)_{i,j} \end{aligned}$$

3 Computational Results.

The numerical example studied in this paper is of a doubly-periodic double shear layer. The shear layers are perturbed slightly at the initial time, which causes the shear layers to roll up in time into large vortical structures. The initial conditions are given by

$$u = \begin{cases} tanh(\rho(y - 0.25)), & \text{for } y \leq 0.5; \\ tanh(\rho(0.75 - y)), & \text{for } y > 0.5. \end{cases} \tag{27}$$

$$v = \delta sin(2\pi x), \tag{28}$$

where ρ is the shear layer width parameter, and δ is the size of the perturbation. In all our examples, the perturbation size used is $\delta = 0.05$. The shear layer width is varied to study the effect of the layer resolution on the computations. The time step Δt for the Godunov-projection method is recomputed each step by setting

$$\Delta t = Ch / \max_{ij}(|u_{ij}|, |v_{ij}|)$$

where C is the CFL number whose value for each run is 0.9. The same procedure is used for the centered difference method but with a CFL number of 0.7.

For the Godunov-projection computations, an initial pressure gradient field is required for time level $n = -\frac{1}{2}$. This is determined by an iteration procedure described in [1].

3.1 The reference solutions.

The reference solutions used for the studies discussed below were produced using the vorticity stream-function method described in section 2.3. Convergence studies were performed on a set of calculations using successively finer meshes. The error in these calculations was estimated using Richardson extrapolation. Although the theoretical asymptotic convergence rate of the method is not apparent until the finest meshes, it is apparent from table II that the solution converges as the mesh is refined. The consistency that is apparent in the vorticity contour plots, energy spectrum plots, energy and enstrophy decay plots for all different resolutions indicates the validity of the reference solutions as representations of the true solution of the continuous problem.

3.2 The "thick" shear layer problem.

In this section, we demonstrate that when the double shear layer problem is well-resolved by the computational mesh, the results of the Godunov method are virtually indistinguishable from those obtained with the centered finite-difference method. Figures 2 through 5 show vorticity contours for the smooth shear layer test problem. For this example, a layer width parameter of $\rho = 30$ was used, as in [1]. Figures 2 and 3 show solutions computed using the Godunov-projection method at times 0.8 and 1.2, respectively. Figures 4 and 5 show solutions at the same times, but computed with the centered difference approximation. The oscillatory nature of the under-resolved centered method is apparent in the 64×64 plots. The solutions obtained by the two methods on the two finest grids are visually indistinguishable. The upper two graphs in figures 6 and 7 show the energy and enstrophy decay of the solutions computed on the 512×512 mesh as a function of time. Again, the plots for the two methods are virtually indistinguishable. This illustrates the important point that in spite of the upwind nature of the Godunov advection step, the Godunov-projection method appears no more dissipative than a high-order centered difference method. Figure 6 also shows a graph of the fraction of the total number of cells at which the limiters in the Godunov method are switched "on" as a function of the timestep. There are four curves in the

latter plot corresponding to the four places in the algorithm where the limiters are used at each timestep. The graph showing the incidence of limiter activation in the method is provided to demonstrate that the limiters, which provide some nonlinear dissipation in the method, are, in fact, switching on during these calculations (presumably in the region around the shear layers). It is clear that the limiters are not adversely affecting the quality of the computed solutions. Table I shows the convergence rate estimates for the Godunov method in this calculation, obtained by Richardson extrapolation. As expected, the the method converges at a second order rate on this example.

The energy spectrum plots in figures 6 and 7 show an approximation of the average value of the Fourier transform of the vorticity as a function of the norm of the wavevector k. The approximation used is given by [12]

$$\frac{\hat{\omega}(k) := [\sum_{|\ell-k|<\frac{1}{2}} |\hat{\omega}(\ell_1,\ell_2)|]}{[\sum_{|\ell-k|<\frac{1}{2}} \ell],} \tag{29}$$

where $\ell := |(\ell_1,\ell_2)|$. It is significant that when the two graphs are superimposed, the behavior of the lower wavenumbers is identical to within the resolution of the graphs. The oscillations in the spectra for earlier times are remnants of the symmetry of the initial data for this example. The differences for higher wavenumbers bear some comment: One can safely assume that the spectral decay behavior demonstrated by the fourth-order centered method (figure 7) is a good representation of the true continuous solutions (see *e.g.* calculations in [13],[12]). Because the graphs are made on a *log-log* scale, the deviations for the highest wavenumbers appear quite significant. The spectral plot for the Godunov-projection method in figure 6 shows that there is more energy in the high wave numbers for this method than for the centered method. However, the *log-log* plot tends to overemphasize this effect, and in fact for the relatively short integration times of these simulations, the difference is negligible. Since curves (C) and (D) in the plots are quite similar, it also appears that the energy in these higher wavenumbers saturates at a level four orders of magnitude below the level of the largest components. One still might speculate that the high wavenumber deviation would become significant for very long-time integrations, should one choose to use a Godunov method. We have not investigated this conjecture in detail.

3.3 Generation of spurious vortices in the "thin" shear layer problem.

This section studies a double shear layer problem where the shear layers are apparently not well-resolved. As with the thick shear layer problem, the converged reference solutions show that the correct solution consists of a double shear layer with a single roll-up. (see figures 8 and 9) While the centered method performs badly on this problem when the flow in not well-resolved, the Godunov method always gives smooth solutions that appear to be well-resolved. Convergence studies of the Godunov calculations demonstrate, however, that on coarser grids, additional roll-ups in the shear layer develop. While the energy in these vortices is relatively small compared to the total energy of the solution, they might easily be interpreted to be physical features in the solution, particularly if not studied in the context of more resolved calculations of the same problem.

Figures 8 and 9 show vorticity contours at two different times for a test problem with a thinner shear layer than the example in section 3.2. In this case, a layer width parameter of $\rho = 100$ was used in the initial conditions. The figures show solutions computed with the Godunov-projection method on grids of resolution 128×128, 256×256 and 512×512, and also the reference solution computed using the centered-difference method with resolution 512×512. Figure 8 is for time 0.8; figure 9 is for time 1.2. It is clear that for the coarser resolutions, the appearance of the Godunov solutions is significantly different from the reference solution. In the 256×256 solution, a spurious vortex has formed midway between the periodically repeating main vortex on each shear layer. The 128×128 solution shows three spurious vortices along the shear layer. Unlike a centered method with which it is visually apparent when the method goes "bad" (see *e.g.* the oscillations in the 64×64 resolution plots of figures 4 and 5), visual inspection of, say, the resolution 256×256 plots in figures 8 and 9 without comparison with computations done at other resolutions, would not suggest an unconverged solution. It is only apparent when comparing the solutions to finer grid solutions that as the method converges with decreasing mesh-size, the spurious vortices disappear. Richardson extrapolation estimates of the error also indicate convergence

(see tables III and IV), although not at the second-order rate one might hope for. Tables V and VI present localized convergence results for the thin shear layer problem. In these tables, the error was estimated by comparing the solutions with a 1024×1024 reference solution in a localized region that includes the spurious vortex. It is interesting that until the problem is sufficiently resolved for the spurious vortex to disappear, there is effectively no convergence in this part of the flow. Another somewhat alarming property of the under-resolved solutions is illustrated by the plots of the kinetic energy and enstrophy decay as a function of time for a resolved and an under-resolved solution shown in figure 13. Despite the substantial difference between the the two solutions, the energy and enstrophy plots are nearly indistinguishable which indicates that such plots can not be used as a measure of the reliability of a particular solution.

The appearance of the spurious vortices is not an artifact unique to this particular method. We made several tests of different versions of the Godunov-projection method to verify that these artifacts were not a peculiarity of the particular method we used. In one case, we disabled the limiters, resulting in a strictly upwind centered (Fromm's) method. We also changed the form of the projection operator from the "exact" projection of [10], to an "approximate" projection operator (*cf.* [4]). Neither variation produced any noticeable difference in the results. Both Rider [14] and Henshaw [15] report observing similar artifacts using a Lax-Wendroff method and a centered fourth-order difference primitive variable-based method [16], respectively. The beginnings of a spurious rollup are evident as well in some of the published calculations of E and Shu [8] using an ENO method. In figure 10 we show a computation with the centered-difference vorticity stream-function method of the present paper in which spurious vortices are clearly formed in an under-resolved computation of the thin shear layer problem. The method becomes unstable shortly after the time of the second plot in that figure. A similar type of phenomena occurs with the point vortex method when not regularized appropriately. In that method for incompressible flow simulation, computer roundoff can cause spurious rollups to occur, again without any apparent serious breakdown of the method (see [17, 18]).

The appearance of the spurious vortices in these calculations is clearly an under-resolution effect. This is somewhat surprising, since, for example, in figure 8, the shear layer is represented with approximately seven cells across its width at the thinnest point which might normally be considered sufficient resolution for an engineering calculation. However, the following argument demonstrates the validity of this claim. It is well-known that for similar flows, the smallest scale in a two-dimensional Navier-Stokes flow scales with the square-root of the viscosity (see *e.g.* [12]). Thus, artifacts that are due to an under-resolution effect should become more pronounced as the viscosity is decreased, and less pronounced as it is increased. In fact, we would expect that given the results shown in figures 9 and 10, the results of a 128×128 calculation with $\nu = 1/20,000$ should be similar to a 256×256 calculation with $\nu = 1/40,000$. Similarly, a 128×128 calculation with $\nu = 1/10,000$, should be comparable to 256×256 calculation with $\nu = 1/20,000$. This is indeed the case, as shown in figures 11 and 12.

4 Discussion.

Whether or not under-resolved Godunov-projection computations are useful is certain to be a controversial issue. Our objective in this paper was not to decide this issue, but to present a careful study so that users of the method can make informed decisions on the validity of their solutions. Indeed, in realistic engineering situations, the decision of which method to use can often involve complex considerations that are certainly beyond the scope of this paper. In this section we offer some suggestions on how the results of section 3 can be interpreted. The examples presented in that section demonstrate that the behavior of the Godunov-projection method (and indeed any method) for incompressible flow simulations when the solutions are not well-resolved, can differ substantially from physical reality. If one is concerned with studying the detailed behavior of the incompressible Navier-Stokes equations, for example, one must be sure with this method, as with any method, that the solutions are well-resolved by the computational mesh before drawing any conclusions. As we have demonstrated, it is

not sufficient that the computed solutions appear smooth and well-resolved; considered individually, the examples containing spurious vortices attest to this fact. In the cases where the solutions are sufficiently resolved, the Godunov-projection method produces results virtually identical to the reference solution method. We believe that the differences in the energy spectrum plots support the preference of a centered method to the Godunov-method for studies where detailed solution resolution is important. In addition, since the centered methods fail rather badly in the under-resolved case, it is somewhat easier to know when one is properly resolving the computed solutions for those methods. Also, as is well-known, the operation count for a typical centered method is significantly less than for Godunov methods since the calculation of the convective derivatives is so much simpler, even for a spatially fourth-order method, than for a Godunov method. However, as we argued above, the differences in the energy spectra are really not that substantial, and in fact, the similarities between the two types of methods as evidenced in those plots and in the plots of energy and enstrophy, are quite striking. These similarities attest to the fundamental integrity of the Godunov-projection methods.

While the behavior of the Godunov-projection methods on well-resolved problems is important to understand, one must realize that this was not the "design point" for these methods. Godunov methods for approximating the advective terms in the incompressible Navier-Stokes equations were developed with the hope of being able to treat under-resolved problems in a robust and physically meaningful, if not entirely accurate, way. Due to constraints imposed by the size of computers and the cost of computing, the engineer might be forced to resolve only the parts of a flow with the most engineering significance, leaving the less important regions in the flow under-resolved. A significant example of this is with adaptive methods, where it is often routine to lower the resolution in regions where such under-resolution has no influence on the quantities of practical interest [19]. A warning here, however, is that adaptive mesh refinement must be used carefully since abrupt changes in mesh spacing in an under-resolved flow can also introduce perturbations that may cause unphysical features such as spurious

vortices to form in the calculation. It is therefore desirable to have a method that performs well in both regimes of the computation. Thus, while the correct details may be simulated in the more resolved parts of the computation, simply capturing the gross properties of the flow correctly in under-resolved regions may be sufficient. The similarity of the energy, enstrophy and energy spectra of the various under-resolved and resolved examples in the previous section indicate that the Godunov method is, in a certain sense, representing the fluid behavior in a physically meaningful way, even when under-resolving the flow. E and Shu [8] found in their ENO calculations that total circulation was computed correctly in under-resolved situations, and we speculate that this would be the case for the Godunov calculations as well.

It is tempting also to compare these under-resolved computations with the zero-width shear layer computations presented in [1]. In that paper, computations are presented with initial conditions (27) where ρ is effectively set to ∞. Comparisons for pure Euler and various finite Reynolds numbers are presented. The $Re = 5,000$ case in [1] is very similar in appearance to some of the thin shear layer examples in the present paper. As $Re \to \infty$, however, the number of vortices in each layer increases. For the Euler calculations, the authors of [1] observed also that as the mesh is refined, the characteristic wavelength of the small scale structures appears to increase linearly with the wavelength with no apparent convergence in the limit of infinitely small mesh-size. One might speculate that such a breakup of the shear layer is somehow characteristic of incompressible Euler flow, however it would be inappropriate to draw such a conclusion from the computations in [1]. In fact, it is difficult to conceive of how this question might be conclusively addressed using finite difference methods. The present study addressed a somewhat different question, that of the convergence of difference approximations of a shear layer with fixed finite initial width. For each finite Reynolds number, as the mesh-size is decreased, the solution converges to a single periodic vortex. We speculate that the same convergence behavior would be observed for thinner initial shear layers. If this speculation were true, it would suggest that the limiting behavior as both $Re \to \infty$ and $\rho \to \infty$ is just a single vortex roll as with the finite-thickness,

finite Reynolds number cases. Again, this would be difficult to verify numerically with finite-difference methods. On the other hand, the problem of a shear layer perturbed by a single long-wavelength mode might not have substantial physical relevance to begin with. A thorough study of the $Re \rightarrow \infty$ problem should also include the effect of more complex perturbations. This is, of course, beyond the scope of the present paper.

In summary, from an engineer's perspective, we have characterized a type of artifact that may occur in under-resolved calculations with Godunov-projection methods. An understanding of such potential artifacts is important for proper interpretation when making routine simulations, as it would be with any tool in the engineer's toolbox. The evidence we have presented regarding behavior of the gross properties of under-resolved flows might suggest that in certain cases these results might be adequate. Making that judgement is not really the point of the present study, however. This paper simply presents information that can be used along with other considerations to help make reasonable decisions for the particular situation involved.

Time	32-64	rate	64-128	rate	128-256	rate	256-512
0.4	1.34E-2	2.43	2.49E-3	1.89	6.73E-4	1.88	1.82E-4
0.8	7.05E-2	2.62	1.14E-2	2.53	1.98E-3	2.08	4.67E-4
1.2	7.51E-2	2.12	1.72E-2	2.50	3.05E-3	2.20	6.61E-4

Table I: L2-errors and convergence rates for the projection method on the thick shear layer problem. In each case, the error was estimated using Richardson extrapolation between two meshes (columns labeled *e.g.* 32-64). The convergence rate exponent was then estimated from these values by comparing adjacent error estimates (columns labeled "rate").

Time	64-128	rate	128-256	rate	256-512	rate	512-1024
0.4	0.268	3.49	2.38E-2	3.86	1.64E-3	3.29	1.67E-4
0.8	1.83	3.72	0.277	3.53	2.41E-2	3.80	1.74E-3

Table II: L2-errors and convergence rates for the centered difference method on the thick shear layer problem. In each case, the error was estimated using Richardson extrapolation between two meshes (columns labeled *e.g.* 64-256). The convergence rate exponent was then estimated from these values by comparing adjacent error estimates (columns labeled "rate").

Time	32-64	rate	64-128	rate	128-256	rate	256-512
0.4	1.07E-1	0.68	6.67E-2	1.70	2.04E-2	2.77	2.98E-3
0.8	2.39E-1	0.13	2.18E-1	0.51	1.53E-1	2.46	2.78E-2
1.2	1.91E-1	-0.16	2.14E-1	-0.22	2.50E-1	2.01	6.18E-2

Table III: L2-errors and convergence rates for the projection method on the thin shear layer problem with $\rho = 100$ and $\nu = 1/10,000$. In each case, the error was estimated using Richardson extrapolation between two meshes (columns labeled *e.g.* 32-64). The convergence rate exponent was then estimated from these values by comparing adjacent error estimates (columns labeled "rate").

Time	32-64	rate	64-128	rate	128-256	rate	256-512
0.4	1.15E-1	0.58	7.68E-2	1.15	3.45E-2	2.59	5.72E-3
0.8	2.45E-1	-0.15	2.71E-1	0.52	1.89E-1	0.98	9.61E-2
1.2	2.01E-1	-0.18	2.28E-1	-0.29	2.78E-1	0.67	1.74E-1

Table IV: L2-errors and convergence rates for the projection method on the thin shear layer problem with $\rho = 100$ and $\nu = 1/20,000$. In each case, the error was estimated using Richardson extrapolation between two meshes (columns labeled *e.g.* 32-64). The convergence rate exponent was then estimated from these values by comparing adjacent error estimates (columns labeled "rate").

Time	32	rate	64	rate	128	rate	256	rate	512
0.4	2.92	0.29	2.39	1.66	7.57E-1	3.74	5.67E-2	1.66	1.80E-2
0.8	3.57	0.10	3.34	0.18	2.94	1.35	1.15	7.92	4.76E-2
1.2	3.18	-0.07	3.34	0.26	2.78	1.01	1.38	9.71	1.65E-2

Table V: Local L2-errors and convergence rates for the projection method on the thin shear layer problem in the region of the main spurious vortex. In this case, the errors were estimated by comparing with a 1024×1024 reference solution. Problems with $\rho = 100$ and $\nu = 10,000$.

Time	32	rate	64	rate	128	rate	256	rate	512
0.4	3.48	0.13	3.17	0.95	1.64	3.23	1.75E-1	2.54	3.01E-2
0.8	3.83	0.07	3.66	0.12	3.36	0.12	3.09	3.24	3.26E-1
1.2	3.27	-0.11	3.52	0.17	3.12	0.30	2.53	3.33	5.25E-1

Table VI: Local L2-errors and convergence rates for the projection method on the thin shear layer problem in the region of the main spurious vortex. In this case, the errors were estimated by comparing with a 1024×1024 reference solution. Problems with $\rho = 100$ and $\nu = 20,000$.

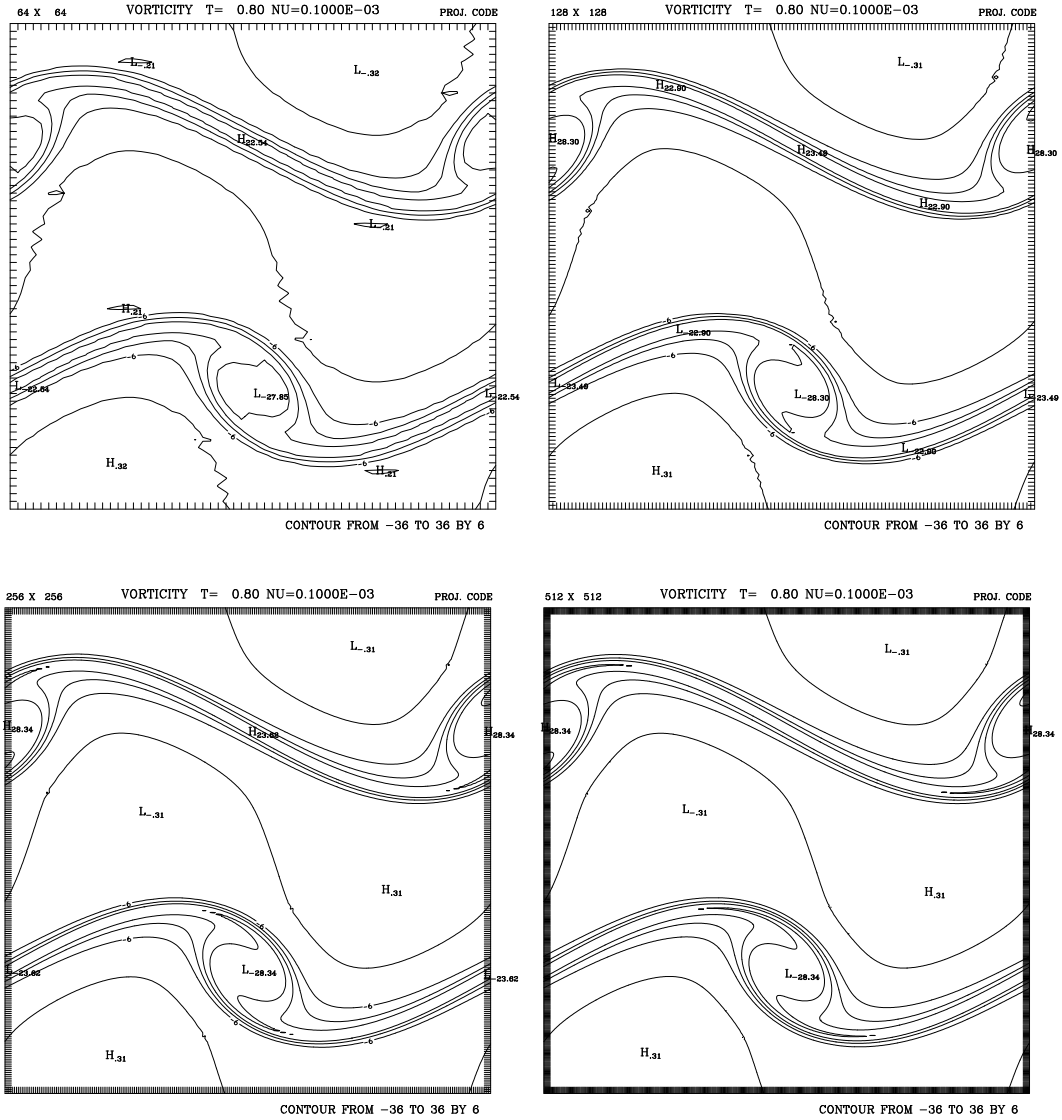

Figure 2: Vorticity contours for the "thick" shear layer at time 0.8 for resolutions 64×64 , 128×128, 256×256 and 512×512 . Godunov-projection method. Layer width parameter $\rho = 30$, viscosity $\nu = 1/10,000$.

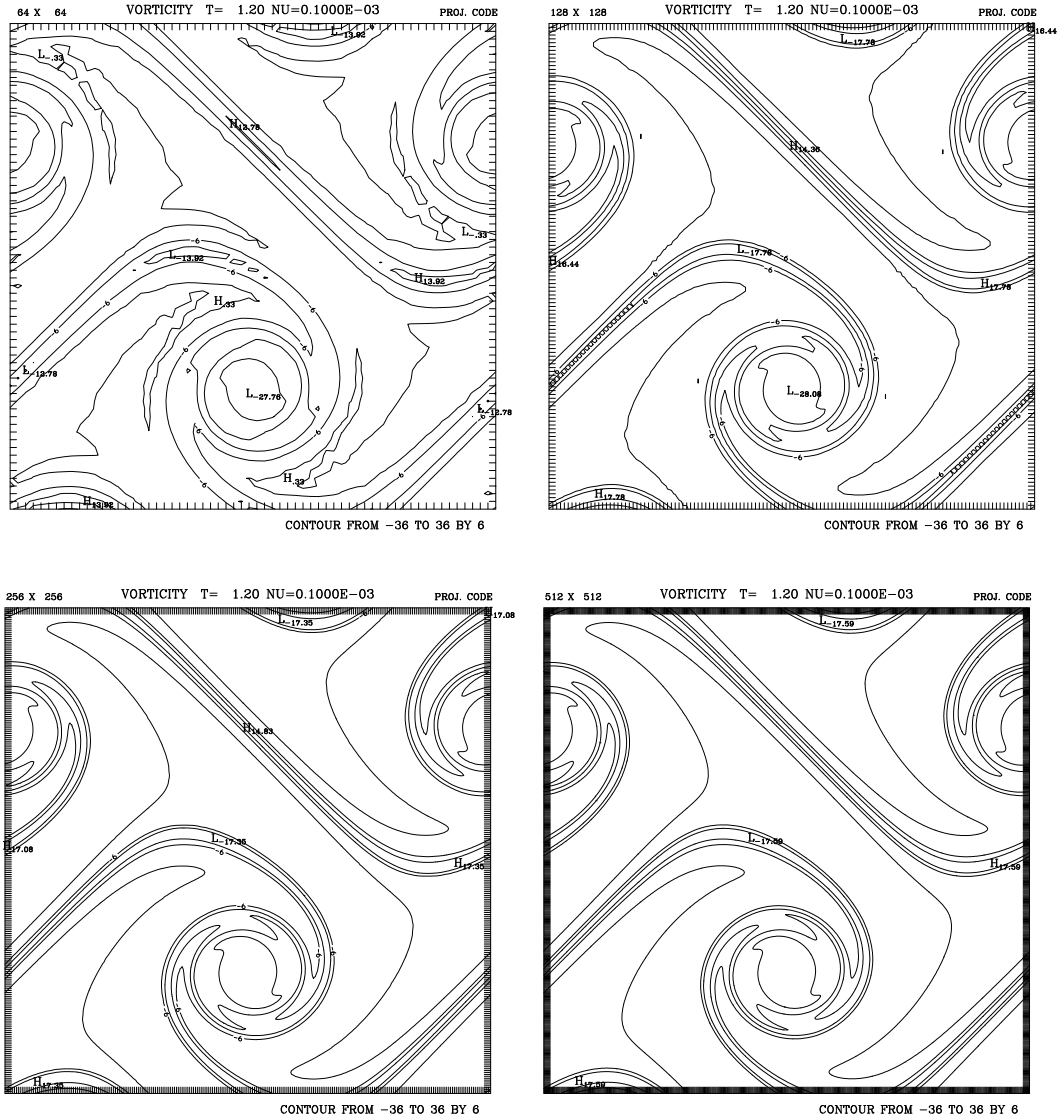

Figure 3: Vorticity contours for the "thick" shear layer at time 1.2 for resolutions 64×64 , 128×128, 256×256 and 512×512 . Godunov-projection method. Layer width parameter $\rho = 30$, viscosity $\nu = 1/10,000$.

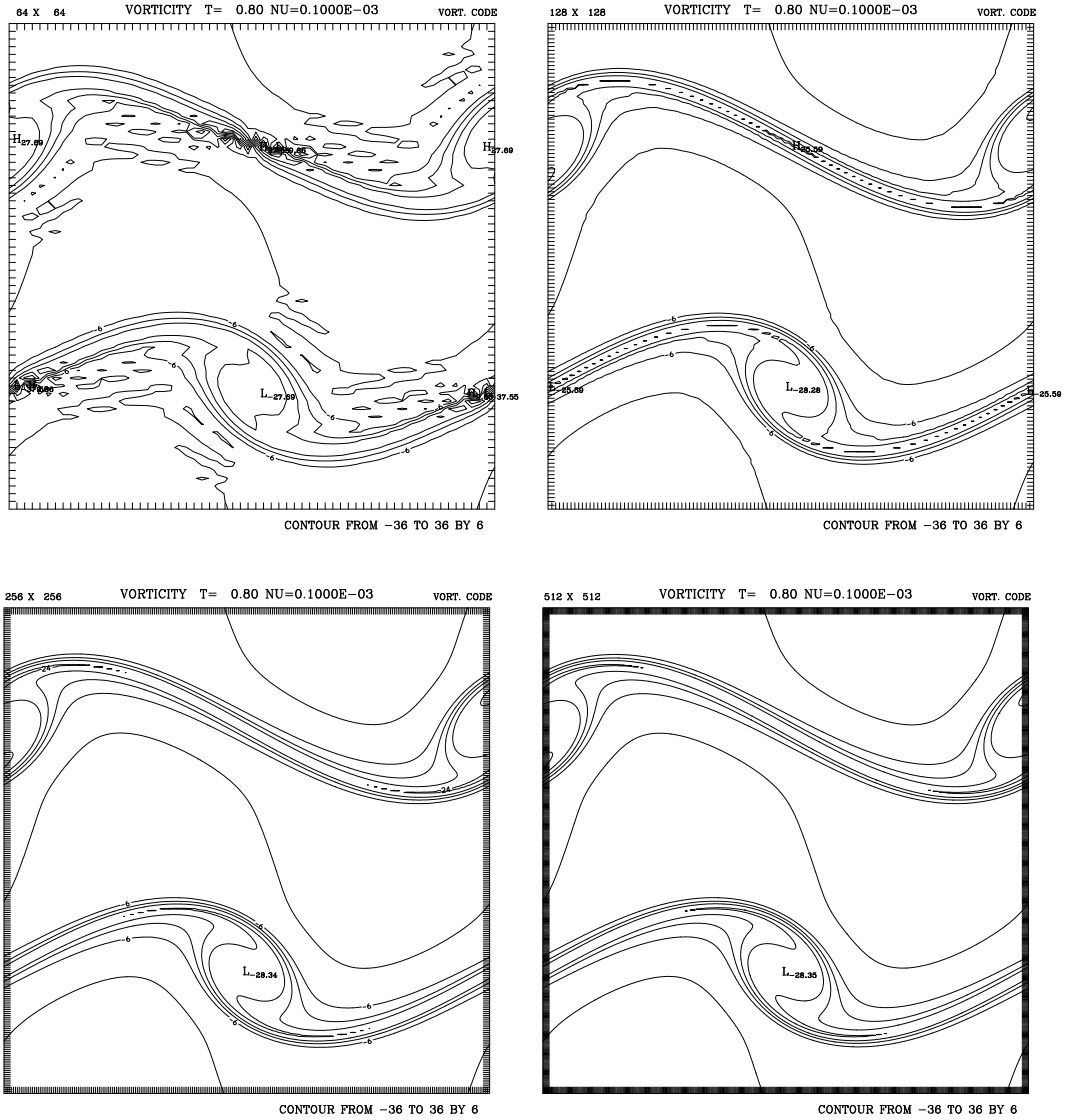

Figure 4: Vorticity contours of the "thick" shear layer problem at time 0.8 for resolutions 64×64 , 128×128, 256×256 and 512×512 . Centered finite-difference method. Layer width parameter $\rho = 30$, viscosity $\nu = 1/10,000$.

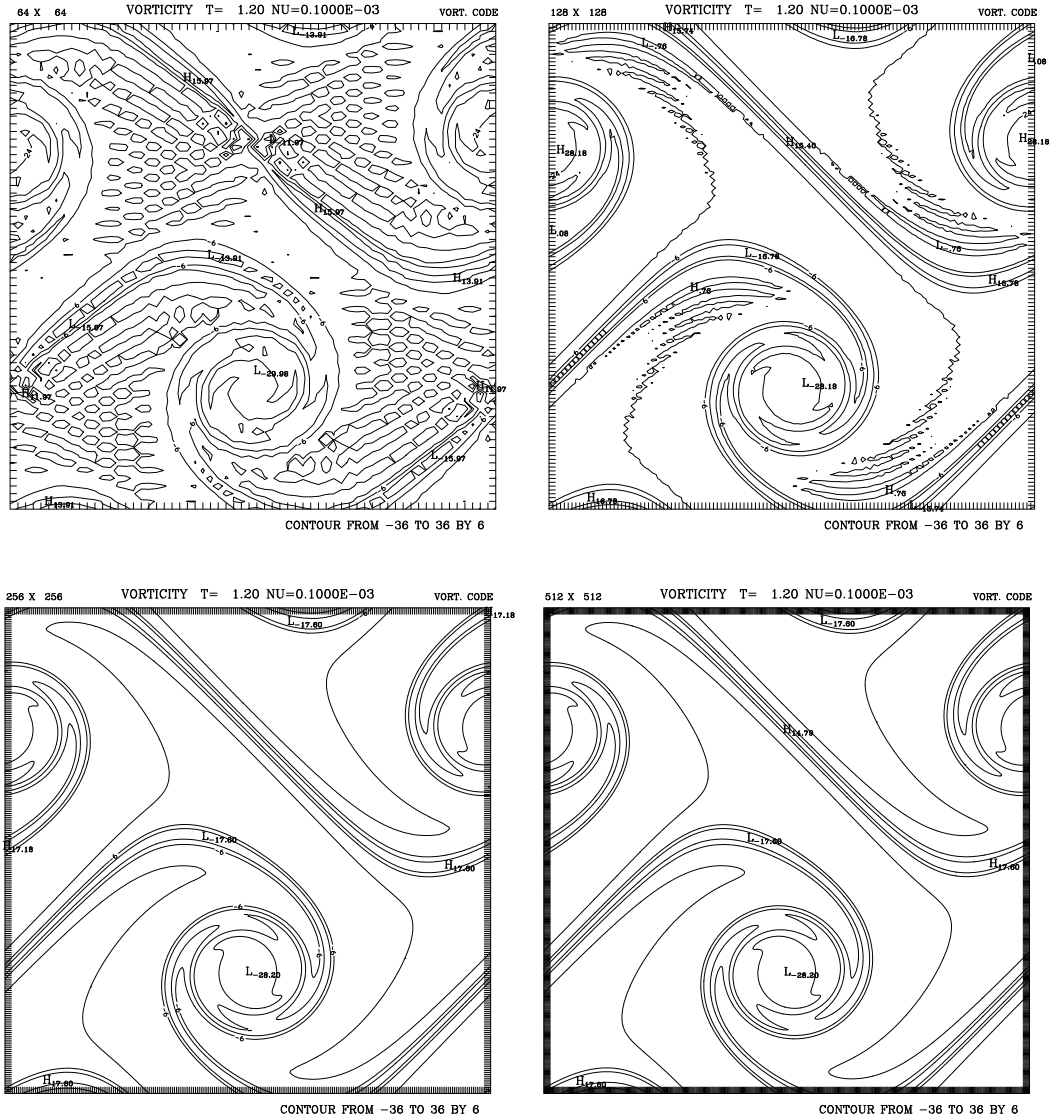

Figure 5: Vorticity contours of the "thick" shear layer problem at time 1.2 for resolutions 64×64 , 128×128, 256×256 and 512×512 . Centered finite-difference method. Layer width parameter $\rho = 30$, viscosity $\nu = 1/10,000$.

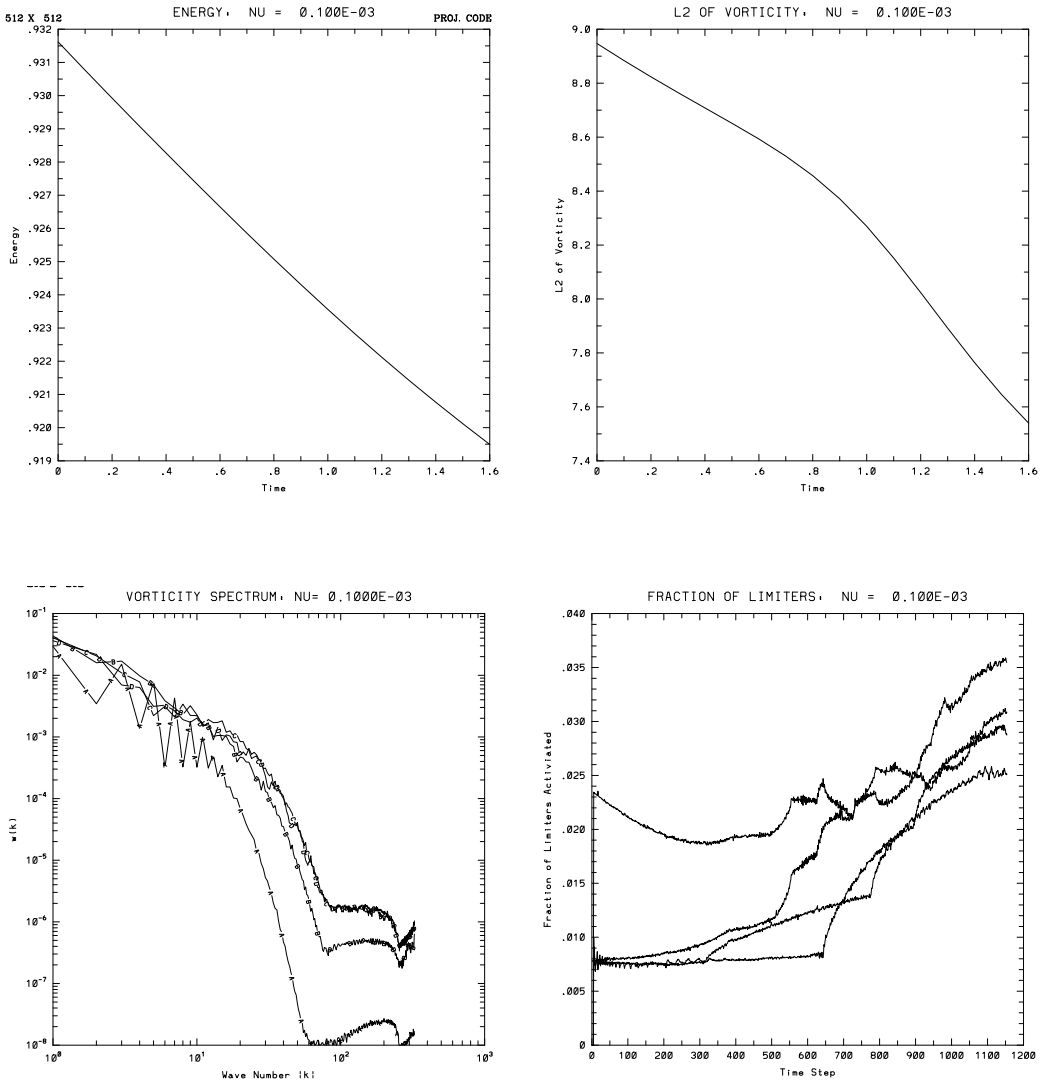

Figure 6: The top two figures show the L_2-norm of the velocity and the L_2-norm of the vorticity as a function of time for the Godunov-projection method. The lower left figure shows plots of the spectrum at times .4(A), .8(B), 1.2(C) and 1.6(D). The lower right figure shows a plot of the fraction of mesh cells at which the limiters switch "on" as a function of time. There are four curves corresponding to the four places in the method at each timestep where the limiters are invoked. All plots are for an example with 512×512 cells, layer width parameter $\rho = 30$, viscosity $\nu = 1/10,000$.

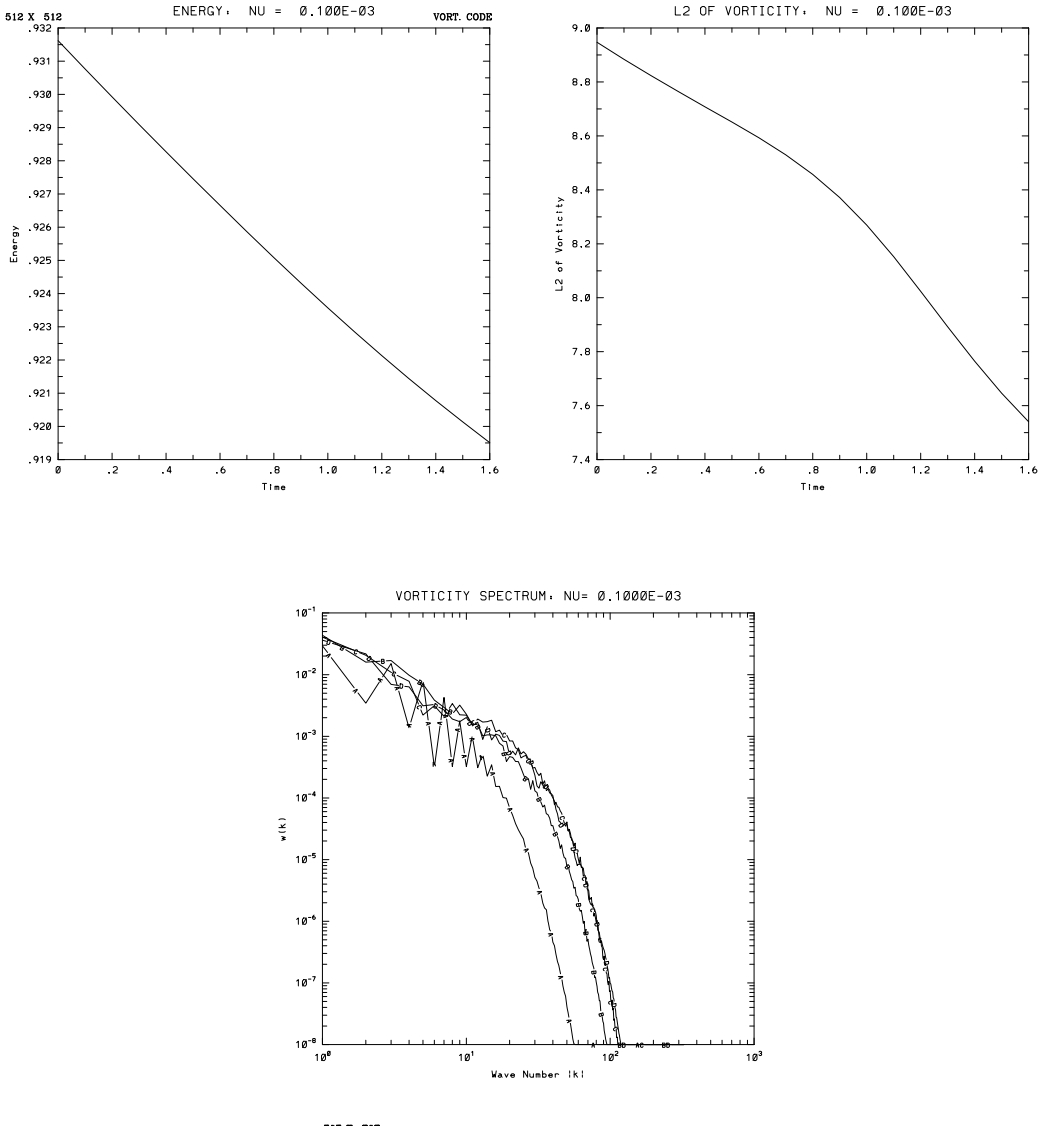

Figure 7: The top two figures show the L_2-norm of the velocity and the L_2-norm of the vorticity as a function of time for the centered finite-difference method. The lower figure shows plots of the spectrum at times .4(A), .8(B), 1.2(C) and 1.6(D). All plots are for an example with 512×512 cells, layer width parameter $\rho = 30$, viscosity $\nu = 1/10,000$.

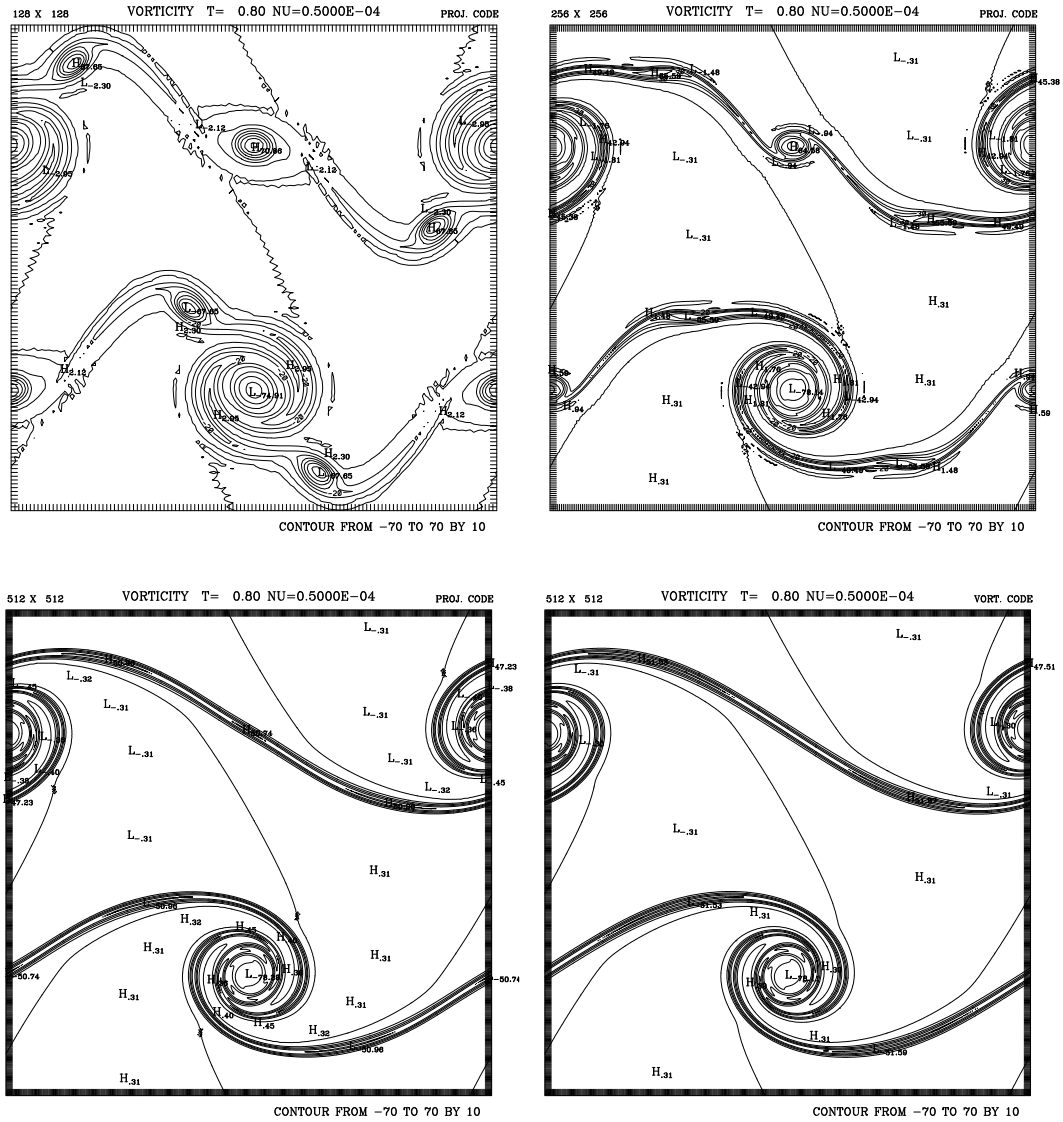

Figure 8: Appearance of spurious vortices for "thin" shear layer problem at time 0.8. From left to right, top to bottom, vorticity contours obtained with the Godunov-projection method with $128 \times 128, 256 \times 256$ and 512×512 cells; Lower right: Centered finite-difference method with 512×512 cells. Layer width parameter $\rho = 100$, viscosity $\nu = 1/20,000$.

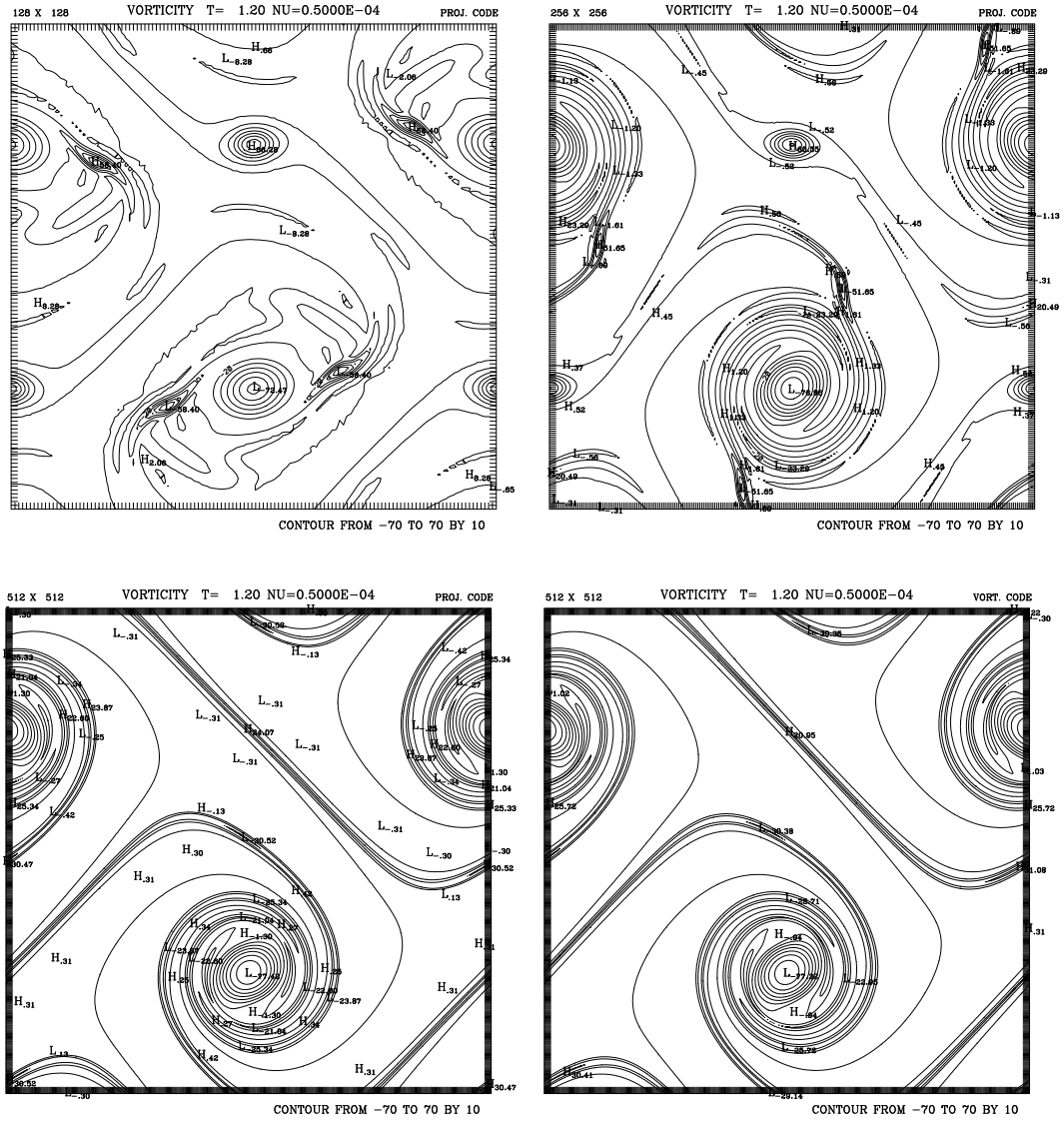

Figure 9: Appearance of a spurious vortex for "thin" shear layer problem at time 1.2. From left to right, top to bottom, Godunov-projection method with 128×128, 256×256 and 512×512 cells; Lower right: Centered finite-difference method with 512×512 cells. Layer width parameter $\rho = 100$, viscosity $\nu = 1/20,000$.

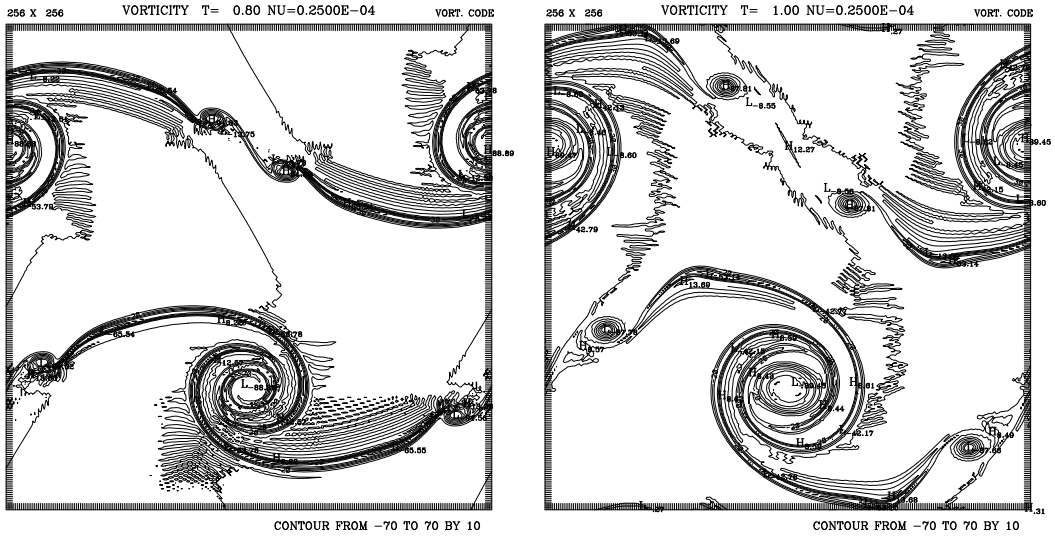

Figure 10: Appearance of spurious vortices for "thin" shear layer problem using the centered finite-difference method. Vorticity contours of the solution at times 0.8 and 1.0. Layer width parameter $\rho = 100$, viscosity $\nu = 1/40,000, 256 \times 256$ cells. The high-frequency oscillations result from the under-resolution of the centered finite difference method and eventually drive the computation unstable.

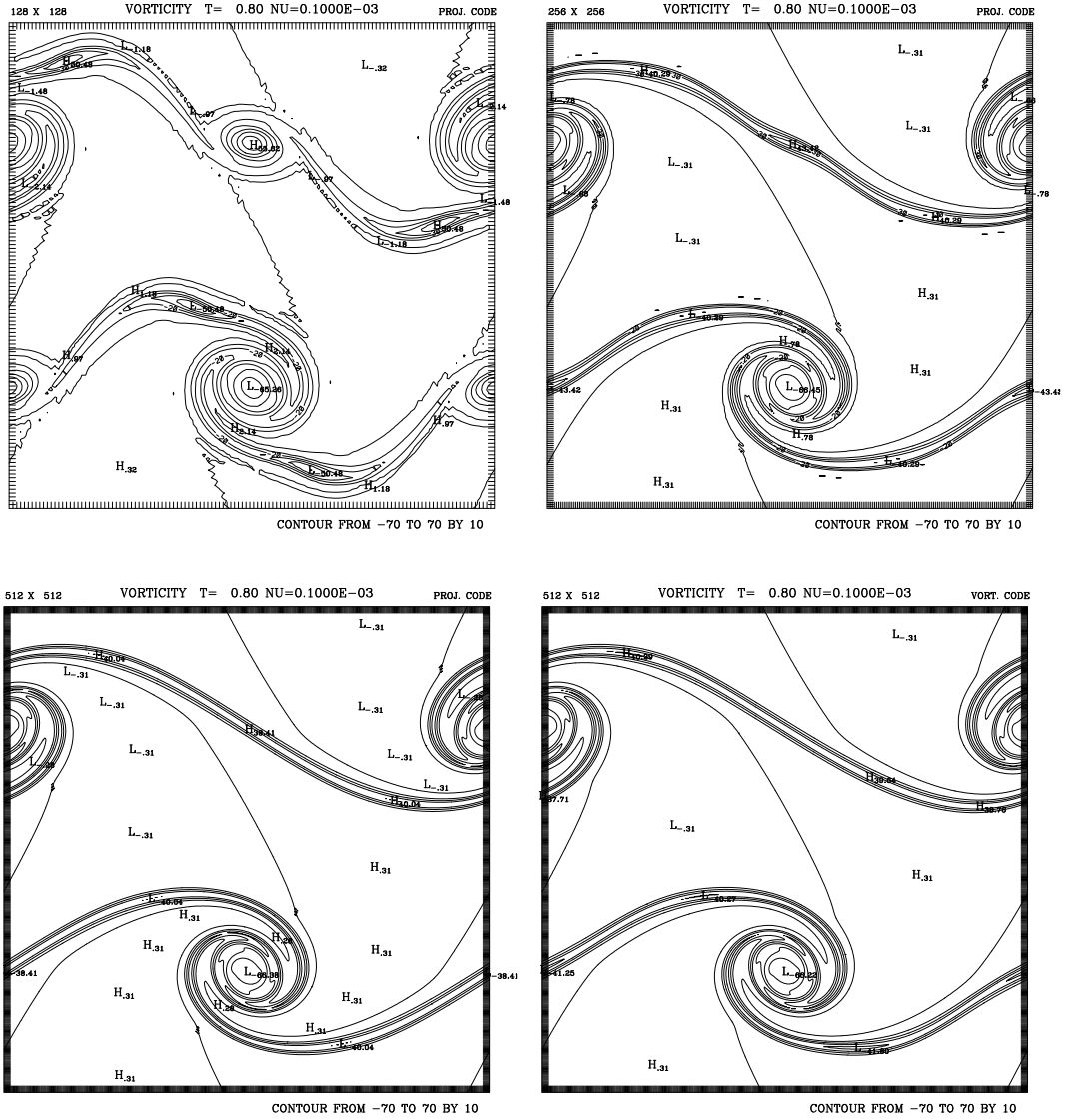

Figure 11: Appearance of a spurious vortex for "thin" shear layer problem at time 0.8. From left to right, top to bottom, vorticity contours for the Godunov-projection method with 128×128, 256×256 and 512×512 cells; Lower right: Centered finite-difference method with 512×512 cells. Layer width parameter $\rho = 100$, viscosity $\nu = 1/10,000$. Viscosity is larger than in figure 8, and so spurious vortices are not as prominent at the corresponding resolution.

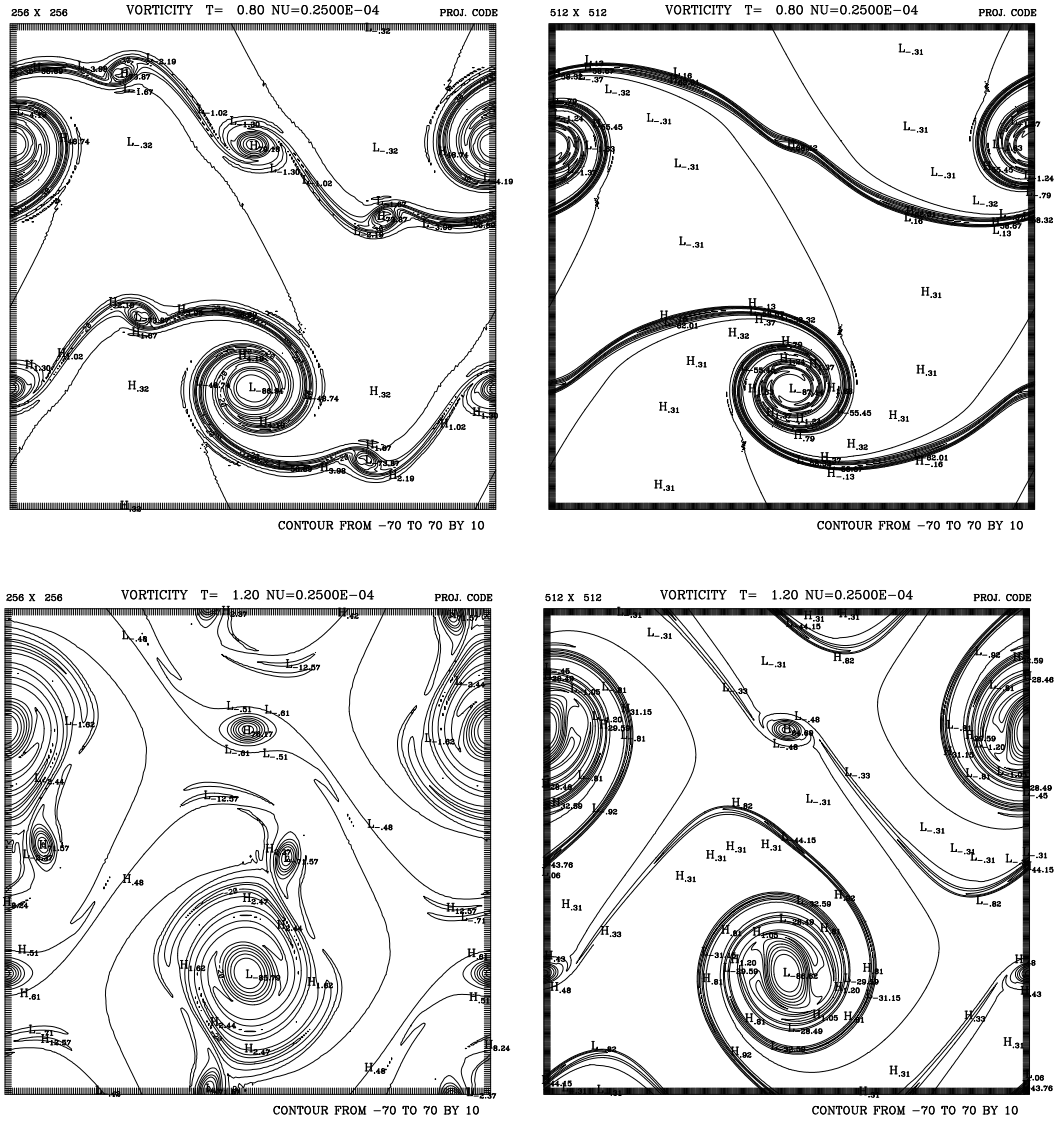

Figure 12: Vorticity contours showing the appearance of a spurious vortex for "thin" shear layer problem at times 0.8 and 1.2. Top: Godunov-projection method with 256×256 and 512×512 cells; time 0.8; Bottom: Godunov-projection method with 256×256 and 512×512 cells; time 1.2; Layer width parameter $\rho = 100$, viscosity $\nu = 1/40,000$. Viscosity is smaller than in figure 8, and so spurious vortices are more prominent at the corresponding resolution.

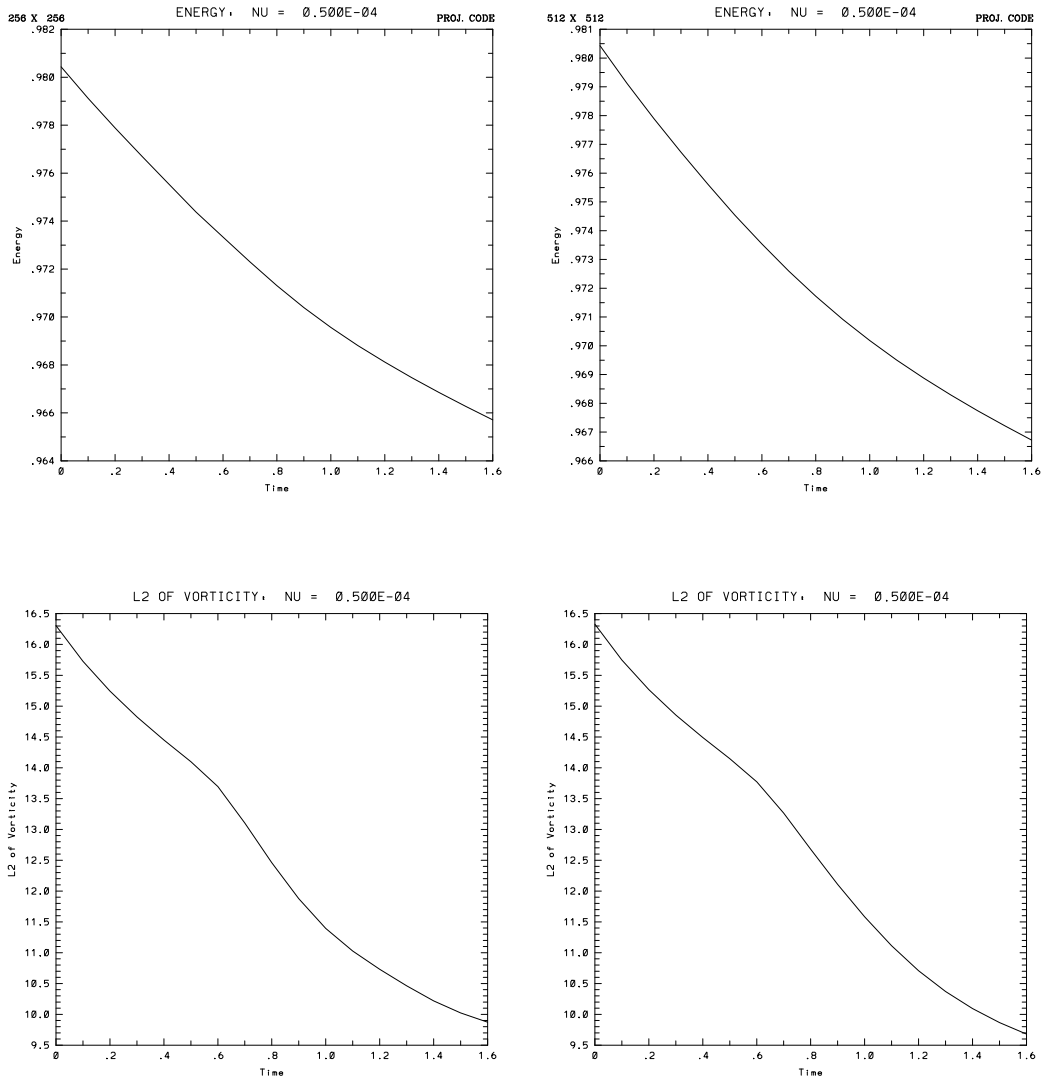

Figure 13: L_2-norm of velocity (top) and L_2-norm of vorticity (bottom) on 256×256 (left) and 512×512 (right) meshes for the example shown in figures 8 and 9. Note that while the 512×512 example appears resolved and the 256×256 example does not, the kinetic energy and enstrophy for the two examples are nearly indistinguishable.

References

[1] J. B. Bell, P. Colella, and H. M. Glaz, *J. Comp. Phys.* **85**, 257 (1989).

[2] A. J. Chorin, *Math. Comp.* **22**, 745 (1968).

[3] P. Colella, *J. Comp. Phys.* **87**, 171 (1990).

[4] A. S. Almgren, J. B. Bell, and W. G. Szymczak, A numerical method for the incompressible Navier-Stokes equations based on an approximate projection, LLNL unclassified report UCRL-JC-112842, Lawrence Livermore National Laboratory, 1993.

[5] M. F. Lai, *A Projection Method for Reacting Flow in the Zero Mach Number Limit*, PhD thesis, University of California, Berkeley, 1993.

[6] M. F. Lai, J. Bell, and P. Colella, A projection method for combustion in the zero Mach number limit, in *Proceedings of the Eleventh AIAA Computational Fluid Dynamics Conference*, pp. 776–783, AIAA, 1993.

[7] A. S. Almgren, J. B. Bell, P. Colella, and L. H. Howell, Adaptive projection method for the incompressible Euler equations, in *Proceedings of the Eleventh AIAA Computational Fluid Dynamics Conference*, pp. 530–539, AIAA, 1993.

[8] W. E and C.-W. Shu, *J. Comp. Phys.* **110**, 39 (1993).

[9] J. B. Bell and D. L. Marcus, *Commun. Math. Phys.* **147**, 371 (1992).

[10] J. B. Bell, P. Colella, and L. H. Howell, An efficient second-order projection method for viscous incompressible flow, in *Proceedings of the Tenth AIAA Computational Fluid Dynamics Conference*, pp. 360–367, AIAA, 1991.

[11] A. J. Chorin, *Math. Comp.* **23**, 341 (1969).

[12] W. D. Henshaw, H.-O. Kreiss, and L. Reyna, *Theoretical and Computational Fluid Dynamics* **1**, 65 (1989).

[13] W. D. Henshaw and H.-O. Kreiss, A numerical study of the propagation of perturbations in the solution of the 2D incompressible Navier-Stokes equations, in *Proceedings of the Third International Conference on Hyperbolic Problems: Theory, Numerical Methods and Applications*, edited by B. Engquist and B. Gustafsson, pp. 544–559, Chartwell-Bratt, 1991.

[14] W. J. Rider, Private Communication, 1994.

[15] W. D. Henshaw, Private Communication, 1994.

[16] W. D. Henshaw, *Journal of Computational Physics* **113**, 13 (1994).

[17] R. Krasny, *J. Fluid Mech.* **167**, 65 (1986).

[18] R. Krasny, *J. Comp. Phys.* **65**, 292 (1986).

[19] P. Colella, Private Communication, 1994.